Chemical Science

EDGE ARTICLE

View Article Online
View Journal | View Issue

Cite this: *Chem. Sci.*, 2018, **9**, 4708

Design of efficient bifunctional catalysts for direct conversion of syngas into lower olefins *via* methanol/dimethyl ether intermediates†

Xiaoliang Liu,[a] Wei Zhou,[a] Yudan Yang,[a] Kang Cheng,*[a] Jincan Kang,[a] Lei Zhang,[b] Guoquan Zhang,[b] Xiaojian Min,[b] Qinghong Zhang*[a] and Ye Wang *[a]

The direct conversion of syngas into lower olefins is a highly attractive route for the synthesis of lower olefins. The selectivity of lower olefins *via* the conventional Fischer–Tropsch (FT) synthesis is restricted to ~60% with high CH_4 selectivity due to the limitation by the Anderson–Schulz–Flory (ASF) distribution. Here, we report the design of bifunctional catalysts for the direct conversion of syngas into lower olefins with selectivity significantly breaking the ASF distribution. The selectivity of C_2–C_4 olefins reached 87% at a CO conversion of 10% and was sustained at 77% by increasing CO conversion to 29% over a bifunctional catalyst composed of Zn-doped ZrO_2 nanoparticles and zeolite SSZ-13 nanocrystals. The selectivity of CH_4 was lower than 3% at the same time. It is demonstrated that the molar ratio of Zn/Zr, the density of Brønsted acid sites of SSZ-13 and the proximity of the two components play crucial roles in determining CO conversion and lower-olefin selectivity. Our kinetic studies indicate that methanol and dimethyl ether (DME) are key reaction intermediates, and the conversion of syngas to methanol/DME is the rate-determining step over the bifunctional catalyst. Formate and methoxide species have been observed on Zn-doped ZrO_2 surfaces during the activation of CO in H_2, and the formed methanol/DME are transformed into lower olefins in SSZ-13.

Received 8th April 2018
Accepted 29th April 2018

DOI: 10.1039/c8sc01597j

rsc.li/chemical-science

Introduction

Lower olefins (C_2–C_4 olefins), which are key building blocks for the manufacture of plastics, cosmetics and pharmaceuticals, are produced by cracking of petroleum-based naphtha in the current chemical industry.[1] The growing demand for lower olefins has motivated a lot of recent research activities for synthesis of lower olefins from alternative carbon resources such as natural gas or shale gas, coal and renewable biomass *via* synthesis gas (syngas, CO/H_2).[2–4] Carbon dioxide can also be used as a renewable source of syngas.[5]

Fischer–Tropsch (FT) synthesis is a classic route for the conversion of syngas to hydrocarbons.[6,7] Many studies have been devoted to synthesizing lower olefins from syngas *via* the FT route on Fe-based or Co_2C-based catalyst.[2,4,7–14] However, the selectivity of C_2–C_4 olefins can hardly exceed 60% due to the limitation by the FT reaction mechanism. Generally, FT synthesis proceeds *via* the dissociation of CO, formation of surface CH_x species ($x = 1$–3), coupling of CH_x species to C_nH_m intermediates and the hydrogenation or dehydrogenation of C_nH_m intermediates to paraffin or olefin products (Fig. 1a).[15–17] The coupling of CH_x species is uncontrollable on surfaces of Fe- or Co-based catalysts, and the hydrocarbon products usually

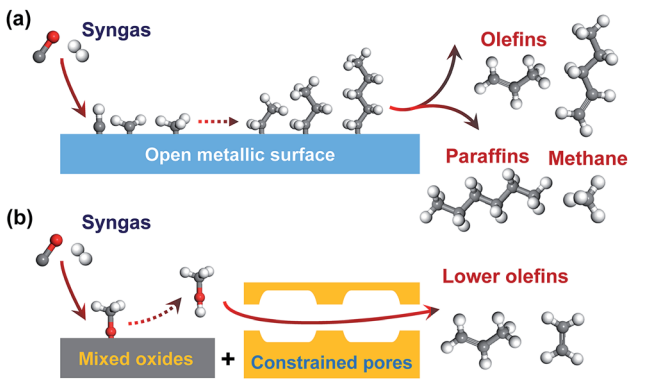

Fig. 1 Illustration of two types of direct conversion of syngas into lower olefins. (a) FT-synthesis route on a Fe-based catalyst. (b) SMO (syngas *via* methanol intermediate to olefin) route on one bifunctional catalyst.

[a]*State Key Laboratory of Physical Chemistry of Solid Surfaces, Collaborative Innovation Center of Chemistry for Energy Materials, National Engineering Laboratory for Green Chemical Productions of Alcohols, Ethers and Esters, College of Chemistry and Chemical Engineering, Xiamen University, Xiamen 361005, P. R. China. E-mail: kangcheng@xmu.edu.cn; zhangqh@xmu.edu.cn; wangye@xmu.edu.cn; Fax: +86-592-218-3047; Tel: +86-592-218-7470*

[b]*State Energy Key Lab of Clean Coal Grading Conversion, Shaanxi Coal and Chemical Technology Institute Co., Ltd., Xi'an 710070, P. R. China*

† Electronic supplementary information (ESI) available: Experimental details, interpretation of rate equation from kinetic analysis, supplementary figures and tables. See DOI: 10.1039/c8sc01597j

follow a statistical distribution known as the Anderson–Schulz–Flory (ASF) distribution.[18] The maximum selectivity of C_2–C_4 hydrocarbons (including paraffins and olefins) is 58% according to the ideal ASF distribution.[19]

The conversion of syngas into lower olefins involves a series of elementary steps (at least including CO activation and C–C coupling), and thus cannot be precisely controlled by using one kind of active sites as in FT synthesis. Thus, we have recently proposed a new reaction-coupling strategy for selectivity control in syngas conversion.[20] The idea is to separate CO activation and C–C coupling on different active sites, which are integrated into one bifunctional catalyst. The reaction coupling may enable a better control of each step, in particular the C–C coupling by choosing an active component capable of performing selective C–C coupling. C_2–C_4 olefins can be produced from syngas *via* two consecutive processes, *i.e.*, syngas to methanol (methanol synthesis) and methanol to olefins (MTO). As compared to the two-process route, a single-process using reaction coupling, which we define as the SMO process (Fig. 1b), *i.e.*, the conversion of syngas *via* methanol intermediate into olefins, would be more energy- and cost-efficient. The product selectivity can be tuned by the shape selectivity of molecular sieves. Zeolites with chabasite (CHA) topology are known to be suitable for the selective formation of C_2–C_4 olefins.[21,22]

Actually, some early papers reported the conversion of syngas to hydrocarbons using mixed catalysts composed of a methanol-synthesis component (*e.g.*, Pd/SiO_2 or Cu–Zn oxide) and a zeolite, but the major products were C_2–C_4 paraffins.[23–25] The formation of aromatics was also observed in a few early studies,[26] and the selectivity of aromatics could be significantly enhanced recently through further improving the bifunctional catalyst.[27,28] However, almost no C_2–C_4 olefins were formed in the early work.[23–26] It is likely that C_2–C_4 olefins can easily undergo hydrogenation over the mixed catalysts, and thus the selective formation of C_2–C_4 olefins is a big challenge.

Recently, Jiao *et al.* reported an OX-ZEO process, *i.e.*, the use of a composite catalyst containing a mixed metal oxide ($ZnCrO_x$) and zeolite (MSAPO), for the direct conversion of syngas into lower olefins.[3] The selectivity of C_2–C_4 olefins reached ~80% at a CO conversion of 17% at 673 K under 2.5 MPa of syngas with a H_2/CO ratio of 1.5. They excluded the possibility of methanol as a reaction intermediate and proposed that C_2–C_4 olefins were formed from syngas *via* a ketene (CH_2CO) intermediate.[3] At the same time, we communicated that a bifunctional catalyst composed of ZrO_2–ZnO binary oxide and SAPO-34 could catalyse the conversion of syngas to lower olefins with a selectivity of 74% at 11% CO conversion at 673 K under 1.0 MPa of syngas with a H_2/CO ratio of 2.[29] The selectivity of C_2–C_4 olefins significantly breaks the upper limit of 60% for the conventional FT catalyst. These two pieces of work open a new avenue for the highly selective conversion of syngas beyond the classic FT process. However, the chemistry of this new process, in particular the reaction mechanism, is still unclear.

Here, we report our recent attempt to clarify the key factors that influence the catalytic behaviours of the bifunctional system. We adopt SSZ-13, an aluminosilicate zeolite with the same CHA-topology as SAPO-34, as the active component for the selective coupling of the intermediate to form C_2–C_4 olefins. Similar to SAPO-34, SSZ-13 is an efficient catalyst for the MTO reaction.[30,31] Furthermore, SSZ-13 has attracted much attention as a commercial catalyst for the selective catalytic reduction of NO_x with NH_3 because of its high structural stability.[32] In this work, we first utilize H–SSZ-13 in combination with metal oxides for the direct conversion of syngas into C_2–C_4 olefins. The present work also aims to provide insights into reaction mechanism. The reaction kinetics, reaction intermediates and possible routes for the formation of products (including lower olefins and major by-products) will also be discussed.

Results and discussion

Active components matching with each other for direct conversion of syngas to lower olefins

The use of one bifunctional catalyst to integrate the two reactions in tandem, *i.e.*, syngas to methanol and subsequent MTO is quite challenging. The two reactions typically occur under different reaction conditions; methanol synthesis is operated at temperatures <573 K due to the thermodynamic requirement (Fig. S1a, ESI†), whereas the MTO reaction needs higher temperatures (typically 673–723 K) because of the high activation energy for C–C coupling and the removal of coke deposition.[33] The continuous removal of methanol from methanol-synthesis catalyst by the tandem MTO reaction can overcome the thermodynamic limitation based on Le Chatelier's principle (Fig. S1b, ESI†).[29,34] The equilibrium conversion of CO into lower olefins (C_2H_4 as an example) is ~80% at 673 K and a syngas pressure of 3 MPa (Fig. S1b, ESI†). Thus, the catalyst being capable of selectively producing methanol at ~673 K should be developed. We clarified that methane became a dominant product at 673 K over Cu–Zn–Al oxide, a typical methanol-synthesis catalyst (Fig. S2a, ESI†). Moreover, due to the strong hydrogenation ability of Cu–Zn–Al catalyst, the formed C_2–C_4 olefins were easy to be transformed to C_2–C_4 paraffins by hydrogenation. Almost no C_2–C_4 olefins were obtained on the bifunctional Cu–Zn–Al/SSZ-13–45H catalyst, which composed of Cu–Zn–Al oxide and H–Na–SSZ-13 with a 45% H^+-exchanging degree (denoted as SSZ-13–45H) (Fig. S2b, ESI†). Here, SSZ-13–45H was used as the typical component for C–C coupling in the present work. As already mentioned, many studies by integrating a Cu- or Pd-based methanol-synthesis catalyst with a zeolite only led to the formation of saturated C_2–C_4 paraffins or gasoline-range hydrocarbons from syngas.[23–26,35–37] Therefore, the development of a high-temperature methanol-synthesis catalyst with proper hydrogenation ability is the key to matching the MTO reaction for the synthesis of C_2–C_4 olefins.

We discovered a Zn-doped ZrO_2 (denoted as Zn–ZrO_2) catalyst, which showed high selectivity of methanol and dimethyl ether (DME), a dehydrative product from methanol, from syngas in a wide-temperature range (Fig. 2a). The bifunctional catalyst composed of Zn–ZrO_2 and SSZ-13–45H provided CH_3OH/DME as the major products at <600 K (Fig. 2b), confirming that the zeolite-catalysed C–C coupling of CH_3OH/DME can only take place at higher temperatures. The selectivity of C_2–C_4 olefins increased at the expense of that of CH_3OH/DME

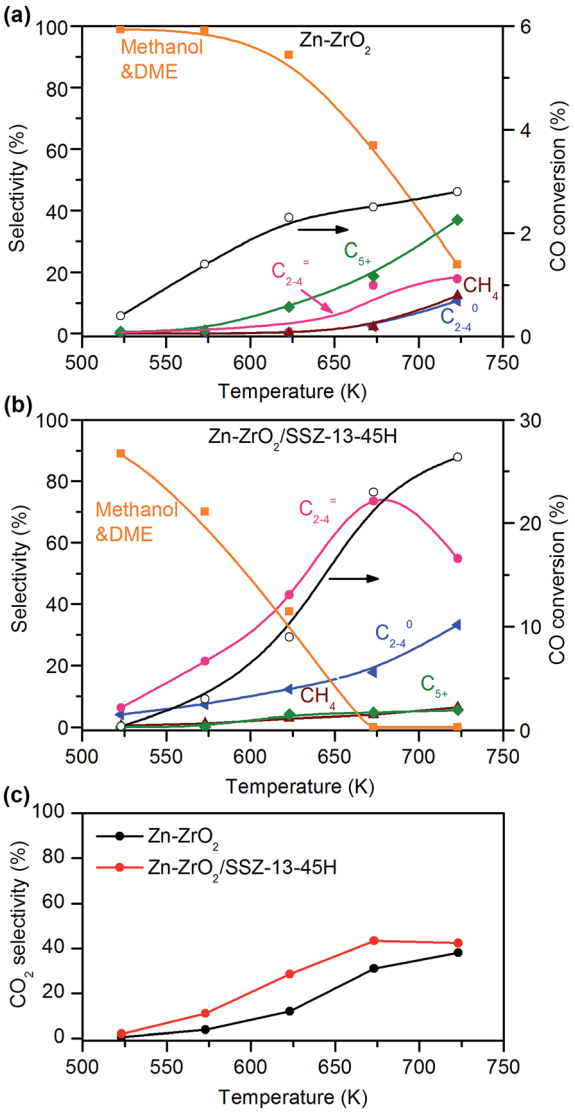

Fig. 2 Catalytic behaviours of Zn–ZrO_2 and Zn–ZrO_2/SSZ-13–45H catalysts for the conversion of syngas at different temperatures. (a) Zn–ZrO_2 (Zn/Zr = 1 : 16). (b) Zn–ZrO_2/SSZ-13–45H. (c) CO_2 selectivity. Reaction conditions: W(Zn–ZrO_2) = 0.20 g; W(Zn–ZrO_2/SSZ-13–45H) = 0.60 g; $H_2/CO = 2$; $P = 3$ MPa; $F = 30$ mL min^{-1}; time on stream, 10 h.

upon increasing the reaction temperature. At the same time, the conversion of CO also increased significantly, becoming much higher than that on the Zn–ZrO_2 catalyst at the corresponding temperature. These observations indicate the transformation of CH_3OH/DME into C_2–C_4 olefins over the SSZ-13 component, which thermodynamically drives the conversion of syngas. The C_2–C_4 olefin selectivity and the CO conversion increased to 75% and 23%, respectively, by increasing the reaction temperature to 673 K (Fig. 2b). A further increase in temperature decreased the selectivity of C_2–C_4 olefins and increased that of C_2–C_4 paraffins due to the hydrogenation of lower olefins.

CO_2 was also formed over both Zn–ZrO_2 and Zn–ZrO_2/SSZ-13–45H catalysts. The selectivity of CO_2 was calculated separately from the hydrogenation of CO and the values depended on reaction temperature (Fig. 2c). The selectivity of CO_2 was slightly higher over the Zn–ZrO_2/SSZ-13–45H catalyst than over the Zn–ZrO_2, but the degree of difference of CO_2 selectivity between the two catalysts was much lower than that of CO conversion.

Key factors controlling the catalytic behaviour of bifunctional catalysts

Effect of composition of Zn-doped ZrO_2. We found that the ZrO_2/SSZ-13–45H catalyst without Zn showed a high selectivity of C_2–C_4 olefins (~80%), but the conversion of CO was very low (Fig. 3). The incorporation of a small amount of Zn (Zn/Zr = 1 : 64) could increase the conversion of CO from 3.9% to 17% without a significant change in the selectivity of C_2–C_4 olefins. The selectivity of C_2–C_4 olefins could keep at 75% with an increase in CO conversion to 23% by raising the Zn/Zr ratio to 1 : 16. A further increase in the ratio of Zn/Zr to ≥1 : 4 considerably decreased the selectivity of C_2–C_4 olefins and increased that of C_2–C_4 paraffins, indicating that the hydrogenation of lower olefins became significant on catalysts with Zn/Zr ratios ≥1 : 4. When the Zn/Zr ratio exceeded 1 : 1, CO conversion also decreased. Thus, the control of Zn/Zr ratio is crucial to both CO conversion activity and product selectivity.

We have performed characterizations to gain insights into the effect of Zn/Zr ratio on structures of Zn–ZrO_2 particles. The X-ray diffraction (XRD) measurements showed that ZrO_2 particles were mainly in the tetragonal crystalline phase with an average size of 6.0 nm (Fig. S3 and Table S1, ESI†). The addition of Zn did not change the crystal structure of ZrO_2 and no diffraction peaks belonging to ZnO were observed from XRD at Zn/Zr ratio of ≤1 : 16. Thus, such a small amount of ZnO may be incorporated into ZrO_2 matrices, forming a solid solution, or may exist as small ZnO clusters on ZrO_2. The formation of ZnO–ZrO_2 solid solution was recently reported.[38] At a higher Zn/Zr

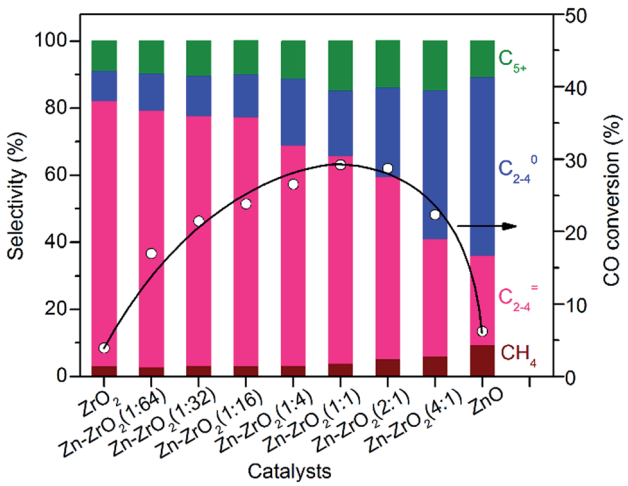

Fig. 3 Effect of Zn/Zr molar ratio on catalytic behaviours of the bifunctional Zn–ZrO_2/H–SSZ-13–45H catalyst. The selectivity of CO_2 did not change with the ratio of Zn/Zr and was in the range of 41–45% for each catalyst. Reaction conditions: catalyst, 0.60 g; $H_2/CO = 2$; $P =$ 3 MPa; $T = 673$ K; $F = 30$ mL min^{-1}; time on stream, 10 h.

ratio (≥1 : 4), diffraction peaks ascribed to hexagonal ZnO became observable (Fig. S3, ESI†). The size of ZrO_2 crystallites estimated by the Scherrer equation from XRD patterns did not change significantly with Zn addition (Table S1, ESI†). The transmission electron microscopy (TEM) measurements showed that the addition of Zn increased the mean size of Zn–ZrO_2 particles (Fig. S4, ESI†). In particular, as the Zn/Zr ≥4 : 1, the mean size of Zn–ZrO_2 particles increased steeply and the size distribution became significantly wide (Fig. S4 and Table S1, ESI†), possibly because of the segregation of large ZnO particles.

Effect of acidity of the zeolite component. To understand the effect of acidity of zeolite SSZ-13 on the catalytic behaviours of the bifunctional catalysts for syngas conversion, we have systematically tuned the density of Brønsted acid sites simply by changing the H^+-exchanging degree. The acidity can be characterized by the NH_3 temperature-programmed desorption (NH_3-TPD) technique. Fig. 4a shows that the intensity of the high-temperature NH_3 desorption peak changes systematically with the H^+-exchanging degree. The high-temperature peak arises from strong acid sites, which may be considered as the Brønsted acid sites in zeolites.[39] The density of strong acid sites evaluated from the intensity of the high-temperature peak increased almost linearly with the H^+-exchanging degree (Table S2, ESI†). We also measured the acidity by the Fourier-transform infrared (FT-IR) spectroscopy of adsorbed NH_3, a small alkaline molecule suitable for probing the acid site in CHA zeolite with small pore windows. Three IR bands at 1633, 1455 and 1405 cm^{-1} were observed (Fig. 4b). The former IR band can be ascribed to the coordination of NH_3 with Na^+, while the latter two splitting bands are assignable to the Brønsted acid sites (protonated NH_4^+).[40,41] The density of Brønsted acid sites evaluated by quantifying the NH_3-adsorbed FT-IR peaks at 1455 and 1405 cm^{-1} was similar to that from the NH_3-TPD measurements (Table S2, ESI†). This confirms that the high-temperature peak in NH_3-TPD profiles corresponds to the Brønsted acid sites.

The bifunctional catalysts containing Zn–ZrO_2 with a Zn/Zr ratio of 1 : 16 and SSZ-13 with different densities of Brønsted acid sites were investigated for the conversion of syngas. The CO conversion increased significantly from 5% to ~25% with the density of Brønsted acid sites (Fig. 5a). The Brønsted acid site is known to catalyse the MTO reaction but is not responsible for CO activation. Thus, the significant increase in CO conversion should stem from the thermodynamic driving force because of the rapid removal of methanol/DME to form lower olefins by the Brønsted acid sites. This was confirmed by the change in product selectivity. CH_3OH and DME were formed as the major

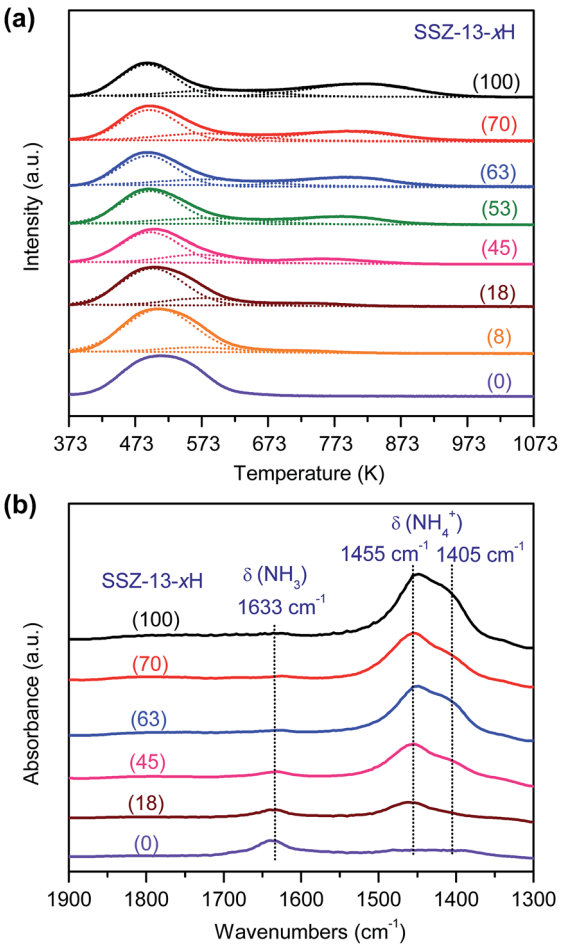

Fig. 4 Characterization of acidity of SSZ-13 with different H^+-exchanging degrees. (a) NH_3-TPD profiles. (b) NH_3-adsorbed FT-IR spectra. The number in the parentheses after each sample denotes the H^+-exchanging degree.

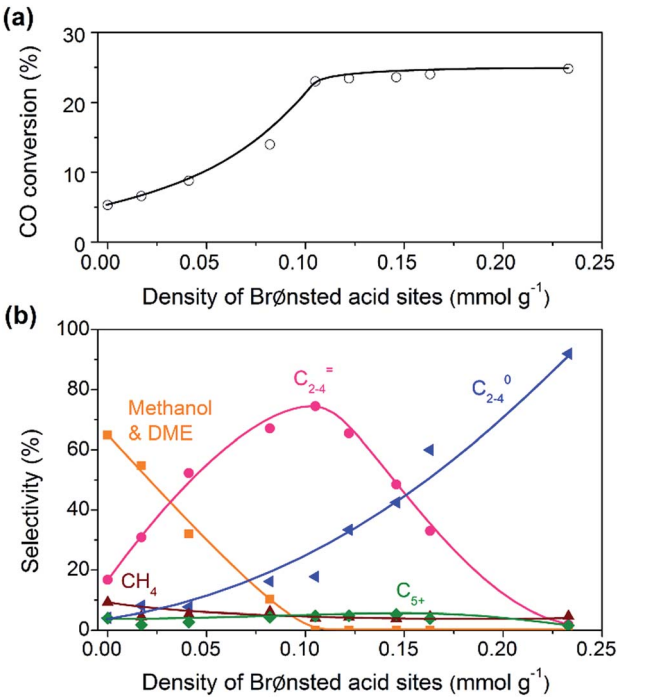

Fig. 5 Effect of density of Brønsted acid sites on catalytic behaviours of the bifunctional Zn–ZrO_2/SSZ-13 catalyst. (a) CO conversion. (b) Product selectivity. The selectivity of CO_2 did not change with the density of Brønsted acid sites and was in the range of 41–45%. Reaction conditions: catalyst, 0.60 g; $H_2/CO = 2$; $P = 3$ MPa; $T = 673$ K; $F = 30$ mL min^{-1}; time on stream, 10 h.

products over the bifunctional catalyst with a lower density of Brønsted acid sites (Fig. 5b). The increase in the density of Brønsted acid sites decreased the selectivity of CH_3OH/DME and increased that of lower olefins. The selectivity of C_2–C_4 olefins reached 75% when the density of Brønsted acid sites rose to 0.10 mmol g^{-1}. However, a further increase in the density of Brønsted acid sites rather decreased the selectivity of C_2–C_4 olefins and increased that of C_2–C_4 paraffins. Thus, there is an optimum density of Brønsted acid sites for the selective formation of lower olefins. These results clearly demonstrate that the Brønsted acidity is a key factor in determining not only the conversion of CO but also the selectivity of lower olefins.

Effect of proximity of the two components. We investigated the effect of the proximity of Zn–ZrO_2 (Zn/Zr = 1 : 16) and SSZ-13 in the bifunctional catalyst on catalytic behaviours. The separation of Zn–ZrO_2 and SSZ-13 by quartz wool in one reactor, *i.e.*, the dual-bed model, led to not only low activity but also decreased selectivity of C_2–C_4 olefins (Fig. 6a). We believe that the low CO conversion is due to the lack of the thermodynamic driving force when the zeolite SSZ-13 is far from the Zn–ZrO_2 or the two components are separated in such a millimetre distance. The high selectivity of CH_4 and C_2–C_4 paraffins probably results from the repeated contact of products with Zn–ZrO_2 in the first bed and SSZ-13 in the second bed, leading to deep hydrogenation and the formation of saturated products instead of lower olefins. The saturated lower paraffins could not be converted on the subsequent zeolite catalyst. The use of mixture of Zn–ZrO_2 granules and SSZ-13 granules with sizes 250–600 μm increases the proximity of the two components to micrometre scale, resulting in significant increases in both CO conversion and C_2–C_4 olefin selectivity (Fig. 6b). The grinding of micrometre-sized SSZ-13 crystallites (Fig. S5, ESI†) with Zn–ZrO_2 powders with a mean particle size of 8.9 nm together, which was typically used in our work, caused the formation of Zn–ZrO_2 nanoparticles dispersed on micrometre-sized SSZ-13 crystallites, and this further increased the conversion of CO and the selectivity of C_2–C_4 olefins (Fig. 6c). To further increase the proximity of the two components, we have synthesized SSZ-13 with a mean size of 230 nm (Fig. S6, ESI†) and Zn–ZrO_2 nanoparticles with a smaller mean size of 4.8 nm by an alcogel method (Fig. S7, ESI†). The grinding of nano-sized SSZ-13 crystallites with powders of Zn–ZrO_2 nanoparticles with mean sizes of 8.9 nm and 4.8 nm further increased the proximity between the two components into nano-scale (Fig. S8, ESI,† 6d and e). The results in Fig. 6 display that the closer proximity between the two components results in higher CO conversion and higher C_2–C_4 olefin selectivity.

We obtained a CO conversion of 29% and a lower-olefin selectivity of 77% over the bifunctional catalyst containing Zn–ZrO_2 nanoparticles with a mean size of 4.8 nm finely dispersed on nano-sized SSZ-13, denoted as Zn–ZrO_2 (4.8 nm)/nano-SSZ-13. This combination of CO conversion and C_2–C_4 olefin selectivity is much better than that reported for our previous catalyst.[29] The selectivity of C_2–C_4 olefins was 71% at 22% CO conversion over the $ZnCrO_x$/MSAPO catalyst at H_2/CO ratio of 2 and 673 K reported by Jiao *et al.*[3] A recently reported MnO/MSAPO catalyst showed a C_2–C_4 olefin selectivity of 79% at CO conversion of 10.1% at 673 K and the increase in CO conversion to 15.4% decreased the C_2–C_4 olefin selectivity to 68.9%.[42] Thus, our present catalyst is outstanding for the direct conversion of syngas into lower olefins. The major by-products in hydrocarbons were C_2–C_4 paraffins and the selectivity of C_2–C_4 paraffins was 18% over our catalyst. We further displayed the detailed selectivities of C_2, C_3 and C_4 olefins and paraffins in Fig. 7a. It becomes clear that propylene with a selectivity of 49% is the most abundant olefin in the product, followed by ethylene (19%) and butenes (8.3%). Among C_2–C_4 paraffins, the selectivity of propane is the highest. The ratios of olefin to paraffin for C_2, C_3 and C_4 hydrocarbons are 3.9, 4.4 and 3.3, respectively. This catalyst was also quite stable during a long-term reaction (Fig. 7b). The CO conversion and C_2–C_4 olefin selectivity were sustained at 25% and 75% after 160 h of reaction. The selectivity of undesired CH_4 was around 3%. The changes in the selectivities of C_2, C_3 and C_4 olefins were also insignificant after 160 h of reaction.

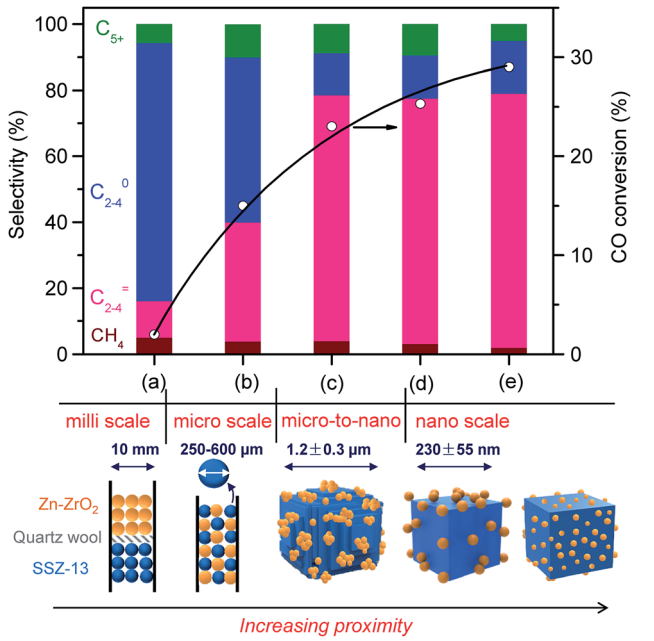

Fig. 6 Effect of proximity of Zn-doped ZrO_2 and SSZ-13 on catalytic behaviours of the bifunctional catalyst. (a) Dual bed (0.20 g Zn–ZrO_2 + 0.40 g SSZ-13–45H); (b) mixing of granules of two components with sizes of 250–600 μm; (c) Zn–ZrO_2 (8.9 nm)/micro-SSZ-13–45H; (d) Zn–ZrO_2 (8.9 nm)/nano-SSZ-13; (e) Zn–ZrO_2 (4.8 nm)/nano-SSZ-13. The selectivity of CO_2 was in the range of 41–45% for each type of proximity. Reaction conditions: catalyst, 0.60 g; H_2/CO = 2; P = 3 MPa; T = 673 K; F = 30 mL min^{-1}; time on stream, 10 h.

Structure–property relationship

The understanding of the roles of ZrO_2 and ZnO in the bifunctional catalyst is crucial to future catalyst design for the conversion of syngas into lower olefins. ZrO_2 is known to be capable of chemisorbing and activating CO.[43] However, the activity of the bifunctional catalyst containing ZrO_2 and SSZ-13 was very low (Fig. 3) probably due to its low capability of

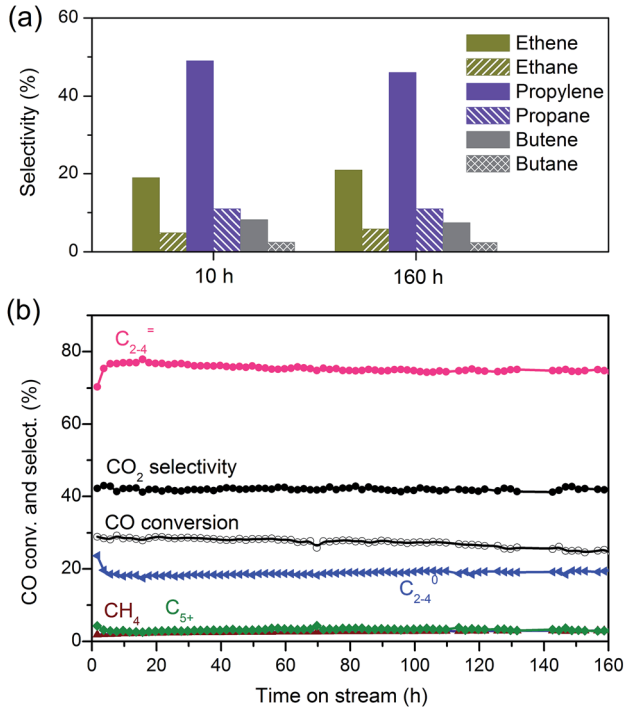

Fig. 7 (a) Selectivities of C_2, C_3 and C_4 olefins and paraffins over Zn–ZrO_2 (4.8 nm)/nano-SSZ-13. (b) Stability of Zn–ZrO_2 (4.8 nm)/nano-SSZ-13 catalyst. Reaction conditions: catalyst, 0.60 g; $H_2/CO = 2$; $P =$ 3 MPa; $T = 673$ K; $F = 30$ mL min^{-1}.

activating H_2. An early report showed that the presence of Cu on ZrO_2 could help H_2 activation and enhance methanol synthesis.[44] Nevertheless, the presence of Cu would accelerate the hydrogenation of lower olefins more significantly, leading to lower paraffins as the predominant products as in the case of Cu–Zn–Al oxide catalyst (Fig. S2, ESI†). One of our most important discoveries is that ZnO is an efficient component for the activation of H_2, offering hydrogen species for the selective hydrogenation of CO with lower olefins surviving. The addition of small amount of Zn could significantly enhance CO conversion while keeping the high selectivity of lower olefins. It is well known that H_2 can be activated *via* heterolytic dissociation on ZnO.[45] The hydrogen species thus formed may be different from those formed *via* homolytic dissociation of H_2 on metallic surfaces. Our result further suggests that the catalyst with –Zn–O– domains incorporated into ZrO_2 lattice or with small ZnO clusters shows higher selectivity of lower olefins, whereas considerable paraffins are formed on catalysts containing larger ZnO particles. Therefore, the unique hydrogenation ability of heterolytically dissociated hydrogen species and their controlled surface concentration are the key to keeping lower olefins from hydrogenation.

The CHA topology of zeolite in the bifunctional catalyst is certainly an important factor for selective formation of lower olefins. Our result reveals that the present SSZ-13 is more selective toward the formation of propylene (Fig. 7a), possibly because the size of pore windows of SSZ-13 matches better with that of propylene molecule. In addition to the topology, the Brønsted acidity is a key parameter. The Brønsted acid site catalyses the C–C coupling, transforming intermediates coming from Zn–ZrO_2 nanoparticles into lower olefins. Although the Brønsted acid site does not directly participate in CO activation, CO conversion can be significantly enhanced by increasing the density of Brønsted acid sites because of the thermodynamic driving force. The product selectivity also depends on the density of Brønsted acid sites; there is an optimum density for the selective formation of lower olefins. Methanol and DME are the major products at a lower density of Brønsted acid sites, while the higher density of Brønsted acid sites results in considerable formation of paraffins. Although zeolites are not typical hydrogenation catalysts, the hydrogenation of olefins on transition-metal-free zeolites has been reported in a few early papers.[46] The catalytic functions of Brønsted acid sites in zeolites for the dissociation of H_2 and the hydrogenation of olefins have also been studied both experimentally and theoretically.[47,48]

How the proximity of the two functional sites affects the catalytic behaviour is a key issue for bifunctional catalysis but has not been well explored so far. A recent study uncovered that the too closer intimacy of Pt nanoparticles and the Brønsted acid sites in HY zeolite was detrimental to the selectivity of hydrocracking products.[49] Our present study suggests that the closer proximity favours CO conversion and C_2–C_4 olefin selectivity. We propose that the closer proximity can enable a faster transfer of reaction intermediates formed on Zn–ZrO_2 nanoparticles to SSZ-13, and thus is beneficial to the selective formation of lower olefins.

Kinetic studies

Activation energy. As shown in Fig. 2, CO conversion activities depended on the reaction temperature over both Zn–ZrO_2 and Zn–ZrO_2/SSZ-13–45H catalysts. The saturation of CO conversion at >673 K on Zn–ZrO_2 is probably due to the thermodynamic limitation. We calculated the apparent activation energy for CO conversion on Zn–ZrO_2 at ≤673 K, where methanol and DME were the major products, using the plot of logarithm of CO conversion rate against the reciprocal of temperature (Fig. S9, ESI†). The value is 72 ± 5 kJ mol^{-1}. CO conversion increased significantly even at >673 K on the ZrO_2/SSZ-13–45H catalyst owing to the thermodynamic driving force. The activation energy for CO conversion on this bifunctional catalyst was calculated to be 71 ± 5 kJ mol^{-1}, almost identical to that on Zn–ZrO_2 catalyst. This suggests that the rate-determining step for the conversion of syngas to lower olefins over the Zn–ZrO_2/SSZ-13–45H catalyst is the same as that for methanol synthesis over the Zn–ZrO_2 catalyst.

Effect of contact time. To gain further information about the reaction pathways, we have investigated the dependence of catalytic performance on the contact time, which is expressed as the ratio of catalyst weight to total flow rate (W/F), at 673 K. CO conversions increased almost linearly with contact time over the Zn–ZrO_2 and Zn–ZrO_2/SSZ-13 (Zn/Zr = 1 : 16) catalysts (Fig. 8). This indicates that the reaction proceeds steadily over both catalysts. CH_3OH and DME were formed as main products over

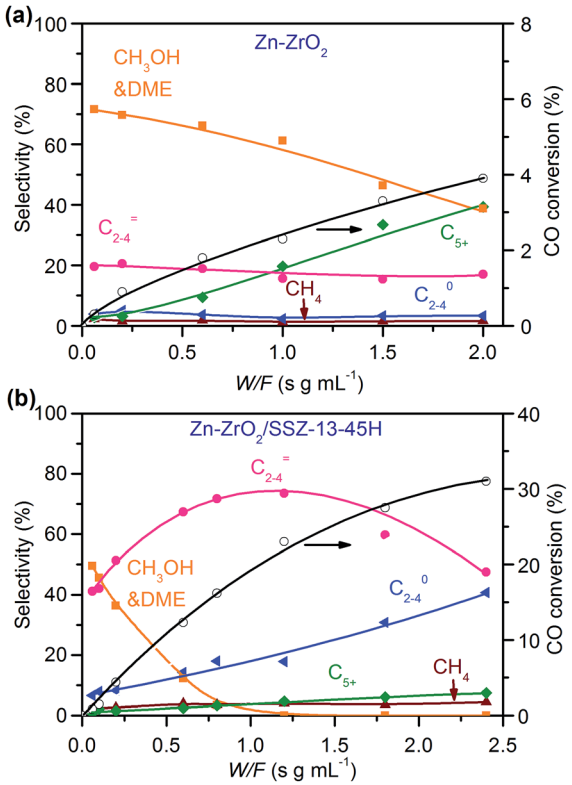

Fig. 8 Effect of contact time on catalytic behaviours of Zn–ZrO_2 and Zn–ZrO_2/SSZ-13–45H catalysts. Reaction conditions: W(Zn–ZrO_2) = 0.030–1.0 g; W(Zn–ZrO_2/SSZ-13–45H) = 0.030–1.2 g; H_2/CO = 2/1; P = 3 MPa; T = 673 K; F = 30 mL min^{-1}; time on stream, 10 h.

the Zn–ZrO_2 catalyst, and the total selectivity of methanol and DME exceeded 70% at shorter contact times. The prolonging of contact time decreased the selectivity of CH_3OH/DME and increased that of C_{5+} hydrocarbons (Fig. 8a). The formation of C_{5+} hydrocarbons at longer contact times may be catalysed by the acid sites on mixed oxides.[50] CH_3OH and DME were also formed as the major products over the Zn–ZrO_2/SSZ-13–45H catalyst at shorter contact time (Fig. 8b). The increase in contact time significantly increased the selectivity of C_2–C_4 olefins at expense of that of CH_3OH/DME. When the contact time exceeded 1.2 s g mL^{-1}, the selectivity of C_2–C_4 olefins decreased and that of C_2–C_4 paraffins increased more significantly due to the hydrogenation of olefins. These results are in agreement with those obtained by changing reaction temperature (Fig. 2b) and the density of Brønsted acid sites (Fig. 5b), providing further evidence that CH_3OH and DME are the reaction intermediates on our bifunctional catalyst. The major reaction pathways for the conversion of CO on the bifunctional catalyst can be expressed as:

$$CO + H_2 \rightarrow CH_3OH/DME \rightarrow C_2\text{–}C_4 \text{ olefins} \rightarrow C_2\text{–}C_4 \text{ paraffins} \quad (1)$$

Effect of syngas pressure. Fig. 9 shows the effect of total pressure of syngas on catalytic behaviours of the Zn–ZrO_2/SSZ-13 catalyst at 673 K and a H_2/CO ratio of 2. At a syngas pressure of 1 MPa, the conversion of CO was 10% and the selectivity of C_2–C_4 olefins was 87% with a ratio of C_2–C_4 olefins/C_2–C_4 paraffins of 9.4. To the best of our knowledge, this is the highest C_2–C_4 olefin selectivity reported to date for the conversion of syngas. Upon increasing the pressure of syngas, the conversion of CO increased significantly but the selectivity of C_2–C_4 olefins decreased. The selectivity of C_2–C_4 paraffins increased at the same time, indicating the increase in the hydrogenation ability at a higher pressure of syngas. The selectivities of minor products, *i.e.*, CH_4 and C_{5+} hydrocarbons, also increased with an increase in the total pressure of syngas. Thus, there exists an optimum total pressure for the conversion of syngas into lower olefins over the bifunctional catalyst.

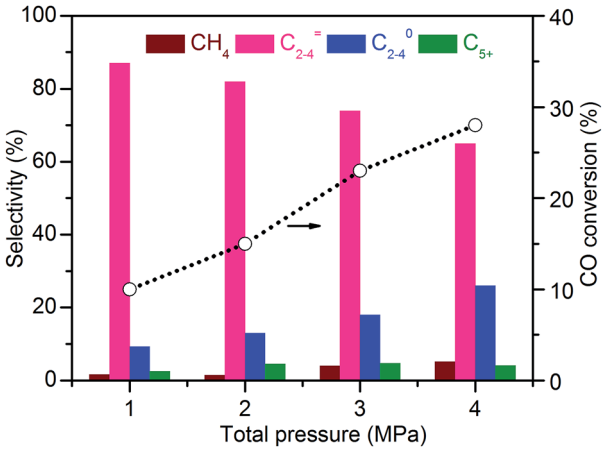

Fig. 9 Effect of total pressure of syngas on catalytic behaviours of Zn–ZrO_2/SSZ-13–45H catalyst. Reaction conditions: catalyst, 0.60 g; H_2/CO = 2/1; T = 673 K; F = 30 mL min^{-1}; time on stream, 10 h.

Effects of CO and H_2 pressures. We have further investigated the effects of partial pressures of CO and H_2, denoted as P(CO) and $P(H_2)$, on catalytic performances over the Zn–ZrO_2/SSZ-13 catalyst at 673 K. In the experiments, the total pressure of syngas was kept at 3 MPa and helium was used as a balance gas to regulate P(CO) while keeping $P(H_2)$ constant or to regulate $P(H_2)$ while keeping P(CO) constant. Fig. 10 shows the dependences of catalytic behaviours of the Zn–ZrO_2/SSZ-13 catalyst on P(CO) at a fixed $P(H_2)$ and on $P(H_2)$ at a fixed P(CO). The rate of CO conversion, denoted as r(CO), showed less than first-order dependence on P(CO) (Fig. S10a, ESI†). We found that the experimental data in Fig. 10a could be fitted to a Langmuir-adsorption model. The plot of P(CO)/r(CO) *versus* P(CO) shows a good linear correlation with a correlation coefficient (R^2) of 0.992 (Fig. 10b). Thus, the rate of CO conversion at a fixed H_2 pressure can be expressed as:

$$r(CO) = k' \frac{K(CO)P(CO)}{[1 + K(CO)P(CO)]} \quad (2)$$

where k' and K(CO) are temperature-dependent constants.

The result on H_2-pressure dependence shows that the rate of CO conversion is less than 0.5-order dependent on $P(H_2)$ (Fig. S10b, ESI†). Our analysis suggests a Langmuir-adsorption

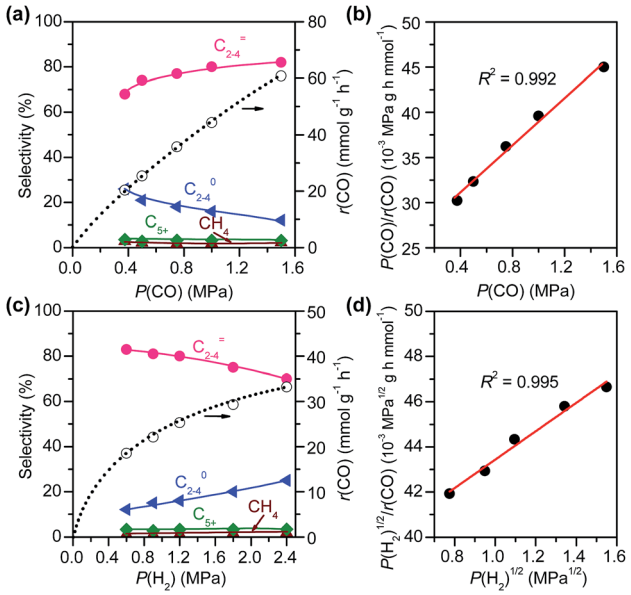

Fig. 10 Effects of pressures of CO and H_2 on catalytic behaviours of Zn–ZrO_2/SSZ-13–45H catalyst. (a) Effect of CO pressure at a fixed H_2 pressure. (b) Plot of $P(CO)/r(CO)$ *vs.* $P(CO)$. Reaction conditions: W = 0.40 g; $P(H_2)$ = 1.5 MPa; T = 673 K; F(total) = 50 mL min^{-1}; P(total) = 3 MPa; time on stream, 10 h. (c) Effect of H_2 partial pressure at a fixed CO pressure. (d) Plot of $P(H_2)^{1/2}/r(CO)$ *vs.* $P(H_2)^{1/2}$. Reaction conditions: W = 0.40 g; $P(CO)$ = 0.6 MPa; T = 673 K; F(total) = 50 mL min^{-1}; P(total) = 3 MPa; time on stream, 10 h.

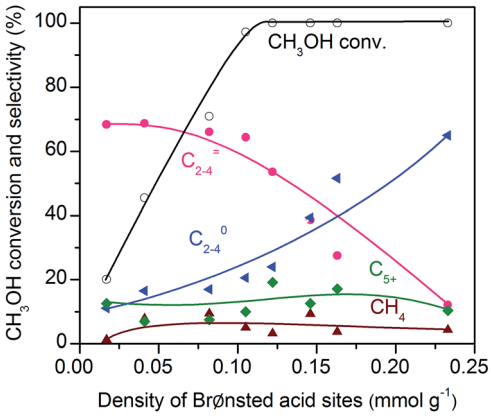

Fig. 11 Effect of density of Brønsted acid sites for the conversion of methanol over SSZ-13 zeolites. Reaction conditions: catalyst, 0.4 g; $F(H_2)$ = 30 mL min^{-1}; F(liquid CH_3OH) = 0.01 mL min^{-1}; P = 2 MPa; T = 673 K; time on stream, 3 h.

model with H_2 dissociatively adsorbed on surface sites; the plot of $P(H_2)^{1/2}/r(CO)$ *versus* $P(H_2)^{1/2}$ could be fitted to a good straight line with a R^2 of 0.995. Thus, the rate of CO conversion at a fixed CO pressure can be expressed as:

$$r(CO) = k'' \frac{K(H_2)^{1/2} P(H_2)^{1/2}}{\left[1 + K(H_2)^{1/2} P(H_2)^{1/2}\right]} \quad (3)$$

where k'' and $K(H_2)$ are temperature-dependent constants.

By combining the results described above, we can express the rate equation of CO conversion as:

$$r(CO) = k \frac{K(CO)P(CO)}{[1 + K(CO)P(CO)]} \frac{K(H_2)^{1/2}\ P(H_2)^{1/2}}{\left[1 + K(H_2)^{1/2} P(H_2)^{1/2}\right]} \quad (4)$$

where k is a temperature-dependent constant.

In addition to the CO conversion rate, the product selectivities are also dependent on the pressures of CO and H_2. A higher pressure of CO favours the selectivity of C_2–C_4 olefins, whereas the increase in H_2 pressure leads to higher selectivity of C_2–C_4 paraffins. This can be explained by the enhancement in hydrogenation of C_2–C_4 olefins at a higher H_2/CO ratio.

Reaction mechanism

To further confirm that CH_3OH is an intermediate, we have performed the conversion of CH_3OH at 673 K under high-pressure H_2 over zeolite SSZ-13 with different densities of Brønsted acid sites. Fig. 11 displays that the conversion of methanol increases with the density of Brønsted acid sites and reaches 97% at a density of Brønsted acid sites of 0.10 mmol g^{-1}. The selectivity of C_2–C_4 olefins was kept at 65–70% when the density of Brønsted acid sites was lower than 0.10 mmol g^{-1}. A further increase in the density of Brønsted acid sites caused the remarkable hydrogenation of C_2–C_4 olefins into C_2–C_4 paraffins. These trends agree well with those observed for the conversion of syngas; methanol/DME can be completely converted as the density of Brønsted acid sites increases to 0.10 mmol g^{-1} and a higher density of Brønsted acid sites would cause the hydrogenation of C_2–C_4 olefins into C_2–C_4 paraffins (Fig. 5). These results provide further evidence that methanol and DME are key reaction intermediates for the formation of lower olefins from syngas over our bifunctional catalysts. Furthermore, the rapid conversion of CH_3OH over the catalyst with an adequate density of Brønsted acid sites agrees well with that the conversion of syngas into CH_3OH/DME is the rate-determining step for the formation of lower olefins over the bifunctional catalyst.

To gain further insights into the adsorbed species on the surfaces of Zn–ZrO_2 nanoparticles, we have performed *in situ* diffuse reflection infrared Fourier-transform spectroscopy (DRIFTS) studies. The adsorption of CO on the pre-reduced Zn–ZrO_2 surface resulted in IR bands at 2974, 2870, 2733, 1594 and 1366 cm^{-1} at 553 K (Fig. 12). These IR bands can be ascribed to surface formate species.[51,52] The intensity of formate species increased as the CO adsorption time increased from 1 to 30 min. The surface hydroxyl groups on metal oxide surfaces have been proposed to participate the formation of HCOO species.[53] Our DRIFTS studies confirmed the existence of multi-coordinated hydroxyl species on fresh Zn–ZrO_2 surfaces (Fig. S11, ESI†). The intensity of the hydroxyl group decreased after the adsorption of CO (Fig. S12, ESI†). This observation confirms the formation of HCOO species through the interaction of CO with surface hydroxyl groups. After switching from CO to CO/H_2, we observed the generation of methoxide species located at 2930, 2820, 1152 and 1052 cm^{-1} together with formate species.[51,52]

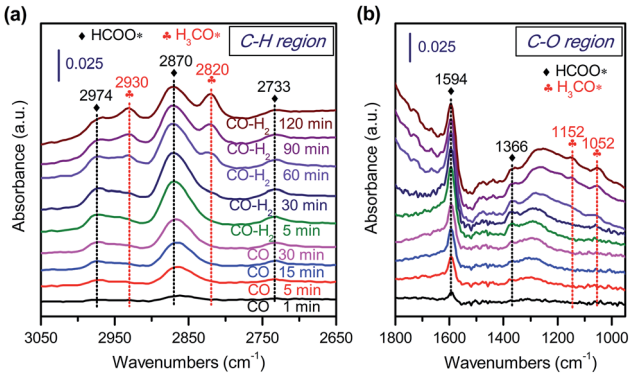

Fig. 12 *In situ* DRIFT spectra for the conversion of CO on Zn–ZrO_2 catalyst. (a) C–H region in 3050–2650 cm^{-1}. (b) C–O region in 1800–1000 cm^{-1}.

The results described above and from literature allow us to speculate a possible reaction mechanism for the hydrogenation of CO on Zn–ZrO_2 surfaces (Fig. 13). ZrO_2 surfaces may activate CO, while H_2 can be heterolytically dissociated on the –Zn–O– domains with H^- bonded to Zn^{2+} and H^+ bonded to O^{2-}.[45,53,54] The surface reaction of adsorbed CO with hydroxyl groups to form formate species should be a facile step as indicated by our *in situ* DRIFT studies (Fig. 12).[55] The hydrogenation of formate species to form methoxide species needs the participation of H species from the heterolytic dissociation of H_2. Based on previous studies,[56,57] we speculate that the H^- species might participate in the hydrogenation of formate, leading to the formation of methoxide species, whereas the H^+ species might be involved in the formation of methanol and the recovery of surface hydroxyl groups (Fig. 13). Methanol can diffuse into the cages of SSZ-13, forming C_2–C_4 olefins catalysed by the Brønsted acid site. The rate equation (eqn (4)) could be interpreted by assuming that the surface reaction between adsorbed CO and dissociatively adsorbed H species on different active sites *via* a Langmuir–Hinshelwood mechanism is the rate-determining step (see details in ESI†). It is noteworthy that the hydrogen species formed by the heterolytic dissociation of H_2 should play a very important role in the selective hydrogenation of CO while keeping lower olefins from hydrogenation. Further experimental and computational studies on the nature of such hydrogen species and their working mechanism are definitely needed in the future work.

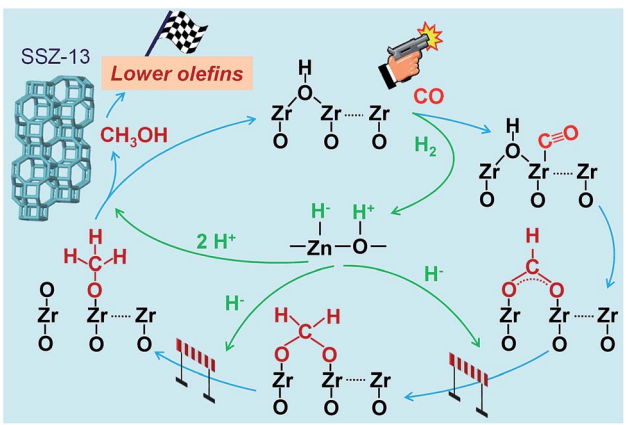

Fig. 13 A possible reaction mechanism for the conversion of syngas into lower olefins over Zn–ZrO_2/SSZ-13 catalyst.

CO_2 was formed as a major by-product over our bifunctional catalyst. We found that the selectivity of CO_2 depended significantly on reaction temperature (Fig. 2c), but it did not change significantly with Zn/Zr ratio, the density of Brønsted acid sites and the proximity of the two components (Fig. 3, 5 and 6). The selectivity of CO_2 was in a narrow range of 41–45% for the bifunctional catalyst at 673 K. Jiao *et al.* also observed the formation of CO_2 with a selectivity of 45% at 673 K over the $ZnCrO_x$/MSAPO catalyst.[3] They proposed that CO_2 was produced by the Boudouard reaction ($2CO \rightarrow CO_2 + C^*$), and the C* was responsible for the formation of CH_2 and CH_2CO (ketene) species in gas phase, which was believed to be the key intermediate for the formation of C_2–C_4 olefins in their system.[3] However, we observed the formation of methoxide species on our catalyst surfaces. Thus, we consider that the breakage of C–O bond does not take place on our Zn–ZrO_2 surfaces but in the cage of zeolite SSZ-13. This is possibly because of the difference in metal oxide catalysts used for CO activation. It is quite interesting that the use of different metal oxides can lead to very different reaction mechanisms.

We speculate that the formation of CO_2 arises from the water–gas shift (WGS) reaction ($CO + H_2O \rightarrow CO_2 + H_2$, $\Delta H^0_{298} = -41$ kJ mol^{-1}), which is kinetically favourable at high temperatures. In fact, both ZnO and ZrO_2 have been reported to be the active catalysts for the WGS reaction.[58,59] We confirmed that the WGS reaction could easily occur on our Zn–ZrO_2 catalyst. The H_2O conversion was >90% at a H_2O/CO molar ratio of ≤2.5/10 (Table S3, ESI†), which was the case on our catalyst by assuming a CO conversion <30%. This approaches the thermodynamic equilibrium for the WGS reaction. By assuming that the WGS reaction arrives at thermodynamic equilibrium over our catalyst, we have evaluated the selectivity of CO_2 contributed solely from the WGS reaction. The result reveals that the selectivity of CO_2 is around 45% at a CO conversion of 10–40% at 673 K (Table S4, ESI†). The selectivity of CO_2 observed experimentally on our Zn–ZrO_2/SSZ-13 catalyst was 43% at 673 K, which is very close to such an estimation. Thus, we believe that the generation of CO_2 over our Zn–ZrO_2-based catalysts is caused by the WGS reaction. The WGS reaction is helpful when the H_2/CO ratio in syngas is low, but this reaction should be inhibited if syngas is produced from natural gas or shale gas. We expect that the design of methanol-synthesis catalyst with suppressed WGS activity may lead to lower CO_2 selectivity.

Conclusions

We have demonstrated that the Zn–ZrO_2/SSZ-13 catalyst efficiently bridges syngas to methanol/DME and methanol/DME to lower olefins. The selectivity of C_2–C_4 olefins reaches 87% at a 10% CO conversion and 77% at a 29% CO conversion at 673 K. Propylene with a selectivity of 49% is the major component in

lower olefins. The bifunctional catalyst is stable during a 160 h of reaction. Our studies point out that the design of a high-temperature methanol-synthesis catalyst with controlled hydrogenation ability is one of the most important keys to realizing the selective formation of lower olefins. As compared to Cu-based catalysts, the Zn-doped ZrO_2 is outstanding in keeping methanol at a high temperature (673 K) and lower olefins from hydrogenation on the bifunctional catalyst under high-pressure H_2. There is an optimum molar ratio of Zn/Zr for the formation of lower olefins. Our work suggests that ZrO_2 works for CO activation, while the –Zn–O– domains or small ZnO clusters are responsible for the activation of H_2 possibly through heterolytic dissociation. The Brønsted acid site in the cages of zeolite SSZ-13 catalyses the C–C coupling to form lower olefins. The density of Brønsted acid sites affects both CO conversion and C_2–C_4 olefin selectivity. An appropriate density of Brønsted acid sites has been found for the selective formation of C_2–C_4 olefins because the hydrogenation of C_2–C_4 olefins also occurs on the Brønsted acid site. The proximity between Zn-doped ZrO_2 and SSZ-13 plays a pivotal role in determining the catalytic behaviours. The closer proximity can facilitate the transfer of reaction intermediates, thus favouring both the activity and lower olefin selectivity. Our kinetic studies strongly indicate that methanol and DME are the key reaction intermediates on our bifunctional catalyst and the formation of methanol/DME is the rate-determining step. We have observed the formation of formate and methoxide species on Zn-doped ZrO_2 surfaces, the precursors of methanol. Our studies also suggest that CO_2, a major by-product, is formed by the water–gas shift reaction. It should be pointed out that although this work provides a reaction-coupling approach for the direct conversion of syngas into lower olefins with high selectivity breaking the ASF distribution, there are still limitations in both the CO conversion and the product selectivity. The formation of CO_2 by the water–gas shift reaction decreases the final yield of C_2–C_4 olefins from CO. The control of hydrogenation ability of Zn-doped ZrO_2 to suppress the hydrogenation of lower olefin products limits the conversion of CO at the same time. The CO conversion obtained in this work is much lower than the equilibrium conversion (~80%). Future studies to improve the CO conversion and to inhibit the generation of CO_2 are needed.

Conflicts of interest

There are no conflicts to declare.

Acknowledgements

This work is supported by the National Key Research and Development Program of Ministry of Science and Technology (2017YFB0602201), the National Natural Science Foundation of China (Nos. 91545203, 21503174, 21433008, 21403177 and 21673188), and Shaanxi Coal and Chemical Technology Institute Co., Ltd.

Notes and references

1 J. J. H. B. Sattler, J. Ruiz-Martinez, E. Santillan-Jimenez and B. M. Weckhuysen, *Chem. Rev.*, 2014, **114**, 10613–10653.
2 H. M. Torres Galvis, J. H. Bitter, C. B. Khare, M. Ruitenbeek, A. I. Dugulan and K. P. de Jong, *Science*, 2012, **335**, 835–838.
3 F. Jiao, J. Li, X. Pan, J. Xiao, H. Li, H. Ma, M. Wei, Y. Pan, Z. Zhou, M. Li, S. Miao, J. Li, Y. Zhu, D. Xiao, T. He, J. Yang, F. Qi, Q. Fu and X. Bao, *Science*, 2016, **351**, 1065–1068.
4 L. Zhong, F. Yu, Y. An, Y. Zhao, Y. Sun, Z. Li, T. Lin, Y. Lin, X. Qi, Y. Dai, L. Gu, J. Hu, S. Jin, Q. Shen and H. Wang, *Nature*, 2016, **538**, 84–87.
5 W. Sheng, S. Kattel, S. Yao, B. Yan, Z. Liang, C. J. Hawxhurst, Q. Wu and J. G. Chen, *Energy Environ. Sci.*, 2017, **10**, 1180–1185.
6 Q. Zhang, J. Kang and Y. Wang, *ChemCatChem*, 2010, **2**, 1030–1058.
7 K. Cheng, J. Kang, D. L. King, V. Subramanian, C. Zhou, Q. Zhang and Y. Wang, *Adv. Catal.*, 2017, **60**, 125–208.
8 H. M. Torres Galvis and K. P. de Jong, *ACS Catal.*, 2013, **3**, 2130–2149.
9 H. M. Torres Galvis, A. C. J. Koeken, J. H. Bitter, T. Davidian, M. Ruitenbeek, A. I. Dugulan and K. P. de Jong, *J. Catal.*, 2013, **303**, 22–30.
10 X. Zhou, J. Ji, D. Wang, X. Duan, G. Qian, D. E. Chen and X. Zhou, *Chem. Commun.*, 2015, **51**, 8853–8856.
11 Y. Cheng, J. Lin, K. Xu, H. Wang, X. Yao, Y. Pei, S. Yan, M. Qiao and B. Zong, *ACS Catal.*, 2016, **6**, 389–399.
12 Y. Cheng, J. Lin, T. Wu, H. Wang, S. Xie, Y. Pei, S. Yan, M. Qiao and B. Zong, *Appl. Catal., B*, 2017, **204**, 475–485.
13 P. Zhai, C. Xu, R. Guo, X. Liu, M. Li, W. Li, X. Fu, C. Jia, J. Xie, M. Zhao, X. Wang, Y. W. Li, Q. Zhang, X. Wen and D. Ma, *Angew. Chem., Int. Ed.*, 2016, **55**, 9902–9907.
14 Z. Li, L. Zhong, F. Yu, Y. An, Y. Dai, Y. Yang, T. J. Lin, S. Li, H. Wang, P. Gao, Y. Sun and M. He, *ACS Catal.*, 2017, **7**, 3622–3631.
15 P. Biloen and W. M. H. Sachtler, *Adv. Catal.*, 1981, **30**, 165–216.
16 R. A. van Santen, I. M. Ciobîcă, E. van Steen and M. M. Ghouri, *Adv. Catal.*, 2011, **54**, 127–187.
17 R. A. van Santen, A. J. Markvoort, I. A. W. Filot, M. M. Ghouri and E. J. M. Hensen, *Phys. Chem. Chem. Phys.*, 2013, **15**, 17038–17063.
18 P. J. Flory, *J. Am. Chem. Soc.*, 1936, **58**, 1877–1885.
19 Q. Zhang, K. Cheng, J. Kang, W. Deng and Y. Wang, *ChemSusChem*, 2014, **7**, 1251–1264.
20 K. Cheng, J. Kang, Q. Zhang and Y. Wang, *Sci. China: Chem.*, 2017, **60**, 1382–1385.
21 U. Olsbye, S. Svelle, M. Bjørgen, P. Beato, T. V. W. Janssens, F. Joensen, S. Bordiga and K. P. Lillerud, *Angew. Chem., Int. Ed.*, 2012, **51**, 5810–5831.
22 P. Tian, Y. Wei, M. Ye and Z. Liu, *ACS Catal.*, 2015, **5**, 1922–1938.
23 K. Fujimoto, H. Saima and H. Tominaga, *J. Catal.*, 1985, **94**, 16–23.

24 K. Fujimoto, H. Saima and H. Tominaga, *Ind. Eng. Chem. Res.*, 1988, **27**, 920–926.
25 Q. Zhang, X. Li, K. Asami, S. Asaoka and K. Fujimoto, *Fuel Process. Technol.*, 2004, **85**, 1139–1150.
26 K. Fujimoto, Y. Kudo and H. Tomonaga, *J. Catal.*, 1984, **87**, 136–143.
27 K. Cheng, W. Zhou, J. Kang, S. He, S. Shi, Q. Zhang, Y. Pan, W. Wen and Y. Wang, *Chem*, 2017, **3**, 334–347.
28 P. Zhang, L. Tan, G. Yang and N. Tsubaki, *Chem. Sci.*, 2017, **8**, 7941–7946.
29 K. Cheng, B. Gu, X. Liu, J. Kang, Q. Zhang and Y. Wang, *Angew. Chem., Int. Ed.*, 2016, **55**, 4725–4728.
30 F. Bleken, M. Bjørgen, L. Palumbo, S. Bordiga, S. Svelle, K. P. Lillerud and U. Olsbye, *Top. Catal.*, 2009, **52**, 218–228.
31 M. A. Deimund, L. Harrison, J. D. Lunn, Y. Liu, A. Malek, R. Shayib and M. E. Davis, *ACS Catal.*, 2016, **6**, 542–550.
32 A. M. Beale, F. Gao, I. Lezcano-Gonzalez, C. H. F. Peden and J. Szanyi, *Chem. Soc. Rev.*, 2015, **44**, 7371–7405.
33 Y. Wei, C. Yuan, J. Li, S. Xu, Y. Zhou, J. Chen, Q. Wang, L. Xu, Y. Qi, Q. Zhang and Z. Liu, *ChemSusChem*, 2012, **5**, 906–912.
34 U. Olsbye, *Angew. Chem., Int. Ed.*, 2016, **55**, 7294–7295.
35 R. A. Dagle, J. A. Lizarazo-Adarme, V. Lebarbier Dagle, M. J. Gray, J. F. White, D. L. King and D. R. Palo, *Fuel Process. Technol.*, 2014, **123**, 65–74.
36 C. Wang, X. Ma, Q. Ge and H. Xu, *Catal. Sci. Technol.*, 2015, **5**, 1847–1853.
37 D. L. S. Nieskens, A. Ciftci, P. E. Groenendijk, M. F. Wielemaker and A. Malek, *Ind. Eng. Chem. Res.*, 2017, **56**, 2722–2732.
38 J. Wang, G. Li, Z. Li, C. Tang, Z. Feng, H. An, H. Liu, T. Liu and C. Li, *Sci. Adv.*, 2017, **3**, e1701290.
39 N. Katada, H. Igi, J. H. Kim and M. Niwa, *J. Phys. Chem. B*, 1997, **101**, 5969–5977.
40 J. Datka, B. Gil and A. Kubacka, *Zeolites*, 1995, **15**, 501–506.
41 F. Yin, A. L. Blumenfeld, V. Gruver and J. J. Fripiat, *J. Phys. Chem. B*, 1997, **101**, 1824–1830.
42 Y. Zhu, X. Pan, F. Jiao, J. Li, J. Yang, M. Ding, Y. Han, Z. Liu and X. Bao, *ACS Catal.*, 2017, **7**, 2800–2804.
43 M. Y. He and J. G. Ekerdt, *J. Catal.*, 1984, **90**, 17–23.
44 K. D. Jung and A. T. Bell, *J. Catal.*, 2000, **193**, 207–223.
45 A. B. Anderson and J. A. Nichols, *J. Am. Chem. Soc.*, 1986, **108**, 4742–4746.
46 M. M. Khabib, S. K. Yu and V. S. Nakhshunov, *Russ. Chem. Rev.*, 1976, **45**, 142–154.
47 J. Kanai, J. A. Martens and P. A. Jacobs, *J. Catal.*, 1992, **133**, 527–534.
48 S. Senger and L. Radom, *J. Am. Chem. Soc.*, 2000, **122**, 2613–2620.
49 J. Zecevic, G. Vanbutsele, K. P. de Jong and J. A. Martens, *Nature*, 2015, **528**, 245–248.
50 Y. Li, D. He, Q. Zhu, X. Zhang and B. Xu, *J. Catal.*, 2004, **221**, 584–593.
51 F. Ouyang, J. N. Kondo, K. Maruya and K. Domen, *J. Phys. Chem. B*, 1997, **101**, 4867–4869.
52 S. Kattel, B. Yan, Y. Yang, J. G. Chen and P. Liu, *J. Am. Chem. Soc.*, 2016, **138**, 12440–12450.
53 N. B. Jackson and J. G. Ekerdt, *J. Catal.*, 1986, **101**, 90–102.
54 S. Kouva, K. Honkala, L. Lefferts and J. Kanervo, *Catal. Sci. Technol.*, 2015, **5**, 3473–3490.
55 K. Maruya, A. Takasawa, T. Haraoka, M. Aikawa, T. Arai, K. Domen and T. Onishi, *Stud. Surf. Sci. Catal.*, 1993, **75**, 2733–2736.
56 H. H. Kung, *Catal. Rev.*, 1980, **22**, 235–259.
57 G. Rossmüller, V. Kleinschmidt, J. Kossmann and C. Hättig, *J. Phys. Chem. C*, 2009, **113**, 1418–1425.
58 D. G. Rethwisch and J. A. Dumesic, *J. Catal.*, 1986, **101**, 35–42.
59 S. Kouva, J. Andersin, K. Honkala, J. Lehtonen, L. Lefferts and J. Kanervo, *Phys. Chem. Chem. Phys.*, 2014, **16**, 20650–20664.